ARTICLE

Spatial tumor biopsy with fluorescence PCR microneedle array

Xiaoxuan Zhang,[1] Guopu Chen,[1] Yu Wang,[1] and Yuanjin Zhao[1,2,3,*]
*Correspondence: yjzhao@seu.edu.cn

Received: June 27, 2023; Accepted: November 13, 2023; Published Online: November 15, 2023; https://doi.org/10.1016/j.xinn.2023.100538

GRAPHICAL ABSTRACT

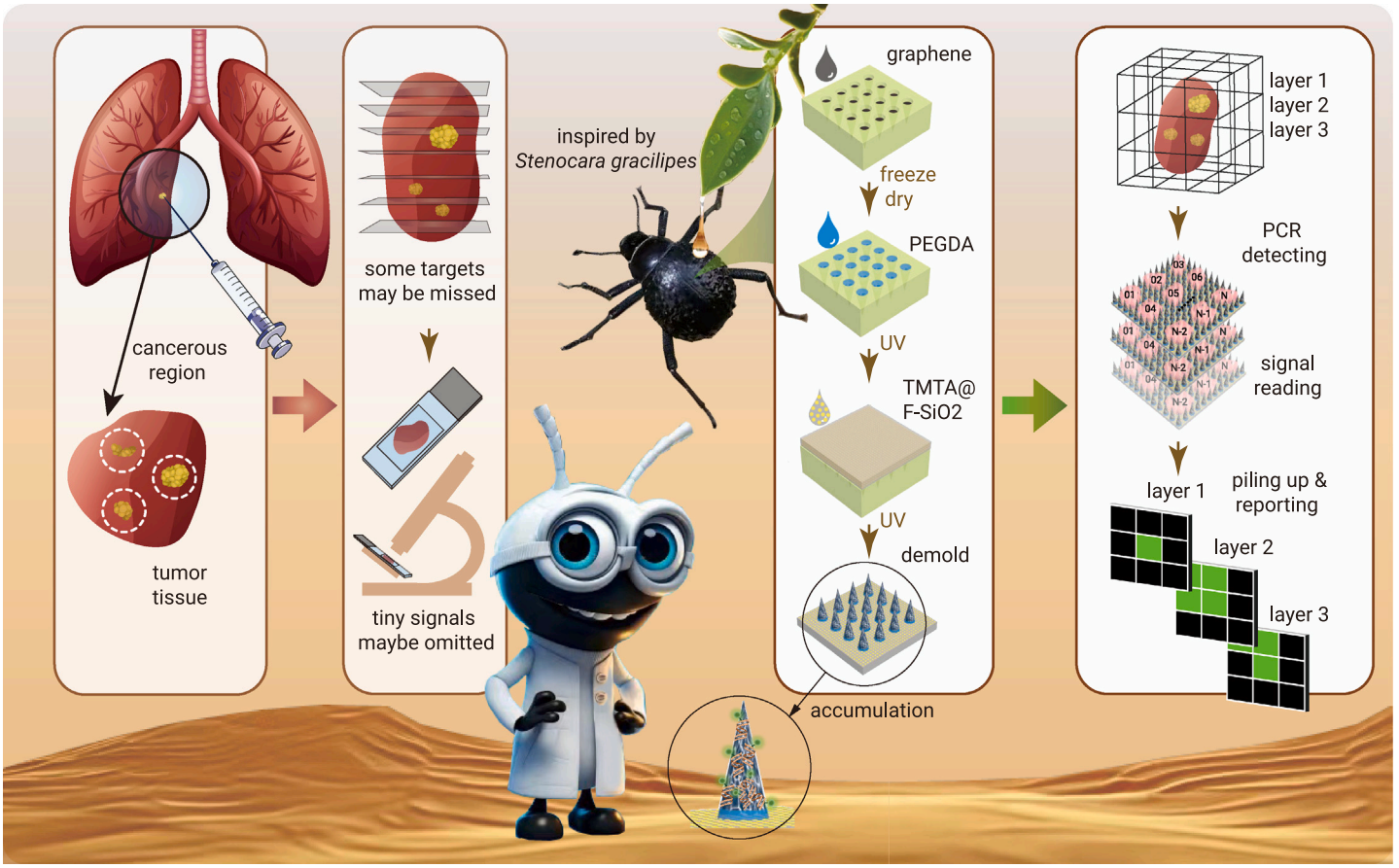

PUBLIC SUMMARY

- Bioinspired microneedle platform with heterogeneous wettability is fabricated.
- Hydrophobic nanoparticle-assembled substrate secludes each needle peak.
- Graphene aerogel hybrid needle peaks collect biomarkers on tissue in a 3D manner.
- PCR reactions are directly conducted on the platform to detect clinical specimens.

ARTICLE

Spatial tumor biopsy with fluorescence PCR microneedle array

Xiaoxuan Zhang,[1] Guopu Chen,[1] Yu Wang,[1] and Yuanjin Zhao[1,2,3,*]

[1]Department of Rheumatology and Immunology, Nanjing Drum Tower Hospital, School of Biological Science and Medical Engineering, Southeast University, Nanjing 210096, China
[2]Oujiang Laboratory (Zhejiang Lab for Regenerative Medicine, Vision and Brain Health), Wenzhou Institute, University of Chinese Academy of Sciences, Wenzhou 325001, China
[3]Chemistry and Biomedicine Innovation Center, Nanjing University, Nanjing 210023, China
*Correspondence: yjzhao@seu.edu.cn

Received: June 27, 2023; Accepted: November 13, 2023; Published Online: November 15, 2023; https://doi.org/10.1016/j.xinn.2023.100538

Citation: Zhang X., Chen G., Wang Y., et al., (2024). Spatial tumor biopsy with fluorescence PCR microneedle array. The Innovation **5(1)**, 100538.

Biopsy is the gold standard for tumor diagnosis, as this technology provides highly detailed and reliable information on tumorigenesis and progression. Resembling the discrete wettability of desert beetles, in this study, a fluorescence polymerase chain reaction (F-PCR) microneedle array (MNA) platform is developed for efficient spatial tumor biopsy. This MNA is fabricated by the coupled strategies of bottom-up self-assembly and top-down photolithography; it comprises a hydrophobic silica nanoparticle-assembled substrate and graphene aerogel-hydrogel hybrid microneedle peaks. Benefitting from the hydrophilicity and absorption capacity of its graphene hybrid microneedle peaks, MNA can easily penetrate tissue specimens and collect tumor nucleic acid biomarkers stereoscopically. In addition, because of the discrete wettability of the platform, both tissue fluids and PCR liquids can be easily removed from the substrate, and each microneedle peak is similar to an independent island for directly conducting F-PCR reactions for tumor marker discovery. Based on these advantages, the F-PCR-MNA platform is demonstrated to be ideal for detecting DNA biomarkers of lung carcinoma in standard solutions, mouse tissue samples, and clinical specimens, thus indicating its practical potential as an innovative tumor biopsy system.

INTRODUCTION

Efficient and precise tumor diagnosis plays a crucial role in the therapy and prognosis of tumors and has considerable clinical significance. In general, imageology[1–4] and blood tests[5–9] are first performed to preliminarily determine the degree of cancerization and cancerous locations; subsequently, tumor biopsy[10,11] is performed for conclusive identification. Biopsy, the gold standard for tumor diagnosis, provides clear, reliable, and detailed pathological information, including cancer type and quality.[12,13] During a traditional biopsy process, first, doctors acquire suspected tissues via surgical excision, forceps, or puncture; then, they comprehensively apply histologic sectioning and tissue staining techniques and ultimately make judgements based on morphological and immunological analysis.[14–16] Despite the high accuracy, the traditional biopsy method is relatively complicated, technology-intensive, and experience-dependent, involves cumbersome procedures, and has a long time cycle. In addition, as traditional biopsy relies on planar tissue slices, it is limited in obtaining overall spatial information, which negatively affects diagnostic results. Therefore, a multidimensional biopsy strategy with satisfactory efficiency and accuracy is highly desired and must be urgently developed.

In this study, a fluorescence polymerase chain reaction (F-PCR) microneedle array (MNA) technology is developed for efficient spatial tumor biopsy; it is shown in Figure 1. This technology comprises microneedles, which feature an array of sharply pointed microsized cones or pyramids, owing to which they can penetrate tissues,[17–19] accumulate interstitial fluids,[20–22] and realize three-dimensional (3D) sampling and detection.[23,24] In particular, each tiny microneedle peak can be regarded as an independent microdomain to conduct non-interacting microbiochemical reactions. By contrast, F-PCR is an emerging biotechnology for nucleic acid amplification and fluorescence signal recognition.[25–27] Owing to its advantages of visibility, convenience, and rapidness, F-PCR has been widely employed in the detection of nucleic acid biomarkers in body fluids,[28–31] such as cell-free DNA (cfDNA) and microRNA (miRNA). Thus, the integration of microneedle devices and F-PCR platforms can form an unprecedented 3D diagnostic system for tissue biomarkers. Microneedles can enable spatial sampling of thick tissue specimens, essentially avoiding cumbersome slicing steps and possible omissions, whereas F-PCR can detect targeted DNA selectively and sensitively and report results quickly and intuitively. However, limited by their current structures and functions, microneedles suitable for F-PCR and a combined system for tumor biopsy remain challenging and unexplored.

In this study, resembling the hydrophilic bulges and hydrophobic back of *Stenocara gracilipes*,[32–35] an anisotropic MNA with discrete wettability is chosen to conduct on-needle F-PCR for spatial tumor biopsy. This anisotropic MNA is fabricated by the coupled strategies of bottom-up self-assembly and top-down photolithography. It comprises a hydrophobic silica nanoparticle-assembled substrate and graphene aerogel-hydrogel hybrid microneedle peaks. Benefitting from the hydrophilicity and absorption capacity of the graphene hybrid microneedle peaks,[36–39] the MNA can penetrate tissue specimens, collect tissue fluids, and quickly capture tumor nucleic acid biomarkers, thereby facilitating stereosampling. Additionally, because of the anisotropic wettability of MNA, both tissue fluids and PCR reaction liquids can be easily removed from the substrate, and each microneedle peak is similar to an independent island for directly conducting F-PCR reactions. Based on these features, the practical value of the F-PCR-MNA technology is demonstrated by spatially screening DNA biomarkers of lung carcinoma in standard solutions, mouse tumor samples, and patient specimens. These results indicate the originality and future prospects of the F-PCR-MNA biopsy system for clinical tumor diagnosis.

RESULTS AND DISCUSSION

The MNA was composed of hydrophilic peaks and a hydrophobic substrate, as shown in Figure 2A. The hydrophilic peaks resembled the hydrophilic bulges of *Stenocara gracilipes*, whereas the hydrophobic substrate resembled the hydrophobic back. Similar to the *Stenocara gracilipes*, which can accumulate water on the hydrophilic bulges, MNA can concentrate liquids on the microneedle peaks. This MNA was fabricated stepwise by replicating a 3D-printed microneedle template (Figure S1). Specifically, a plastic microneedle template was 3D printed, and its shape was transferred to a silicone negative mold through template replication. The 3D-printed microneedle template exhibited a uniform arrangement, with a microneedle height of 500 μm, a microneedle basal diameter of 250 μm, and an intermicroneedle distance of 400 μm, whereas the silicone negative mold exhibited a complementary structure (Figure S2). Using this silicone negative mold, freeze-dried graphene aerogels were inside the cavities to generate microneedle peaks. Polyethylene glycol diacrylate (PEGDA) pre-hydrogels, which possess good mechanical properties, were used to brace the graphene aerogels. After the solidification of the PEGDA pre-hydrogels, a mixture of oleophilic trimethylolpropane triacrylate (TMPTA) pre-polymers and self-assembled hydrophobic-treated silica nanoparticles was added to the microneedle peaks and polymerized to serve as a substrate for expelling water (Figure S1). Finally, the MNA (microneedle height: ~451 μm, microneedle basal diameter: ~228 μm, intermicroneedle distance: ~387 μm) was obtained, and it well duplicated the architecture of the 3D-printed microneedle template, as shown in Figure 2B. Notably, magnified scanning electron microscopy (SEM) images showed the assembly of nanoparticles on the hydrophobic substrate, as well as the distribution of graphene aerogel and PEGDA hydrogel on the microneedle peak (Figures 2C–2E).

Typically, graphene aerogels exhibit poor mechanical strength; thus, a hydrogel brace is required to support the aerogels, ensure tissue penetration, and connect the microneedle peaks to the hydrophobic substrate. To evaluate the function of the hydrogel braces, compression tests were conducted by pressing graphene aerogel-hydrogel brace mixtures or pure graphene aerogels and simultaneously recording the real-time forces (Figure S3). With the combination of PEGDA hydrogel braces, the maximum compression force increased by nearly five times, thus indicating a distinctively improved mechanical strength (Figure S4). Note that to facilitate liquid accumulation at the microneedle peaks and reduce background fluorescence interference, the substrates should be endowed with hydrophobic properties. Therefore, silica nanoparticles were grafted

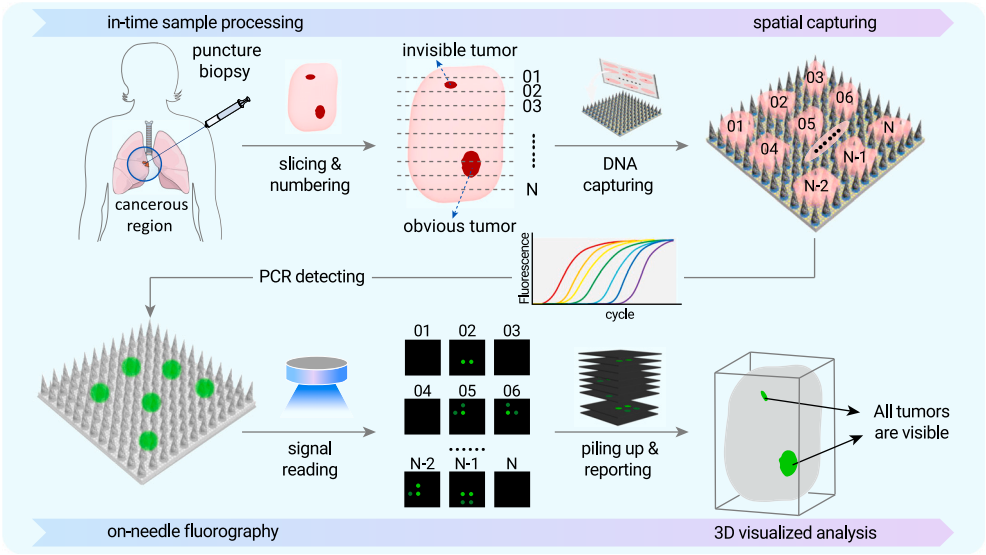

Figure 1. Schematic illustrations of procedures of the spatial tumor biopsy by the F-PCR-MNA The procedures mainly include in-time sample processing, spatial DNA biomarker capturing, on-needle fluorography, and further analysis.

with fluorosilane before dispersion in oleophilic TMPTA pre-polymers. The above dispersions were then solidified to act as substrate materials. Subsequently, contact angle tests were performed to investigate the wettability changes of these substrates compared with those of pure TMPTA and PEGDA plates. Evidently, the contact angle of the substrate was the largest among the three, thus confirming its enhanced hydrophobicity (Figure S5). In addition, water droplets could easily slide down the slanted hydrophobic substrate within 1 s, whereas they spent more than 30 s on the TMPTA plate and were almost pinned on the PEGDA plate (Figure 2F). In addition, the microneedle peaks could pick up red fluorescent droplets, with little water sticking to the substrate after being dipped in water (Figures 2G and 2H).

Owing to their porous structure, large specific surface area, and abundant intermolecular forces, graphene aerogels are adept at absorbing molecules such as DNA.[37,39] Consequently, the graphene aerogels attached to the microneedle peaks can impart MNA with a distinctive DNA capture capacity. In addition, the graphene aerogel occupies a large portion of the microneedle peaks and provides abundant biomolecular adsorption sites. To demonstrate this, microneedles with and without graphene aerogels were cultivated in solutions containing different concentrations of fluorescence-labeled DNA. The microneedles without graphene aerogels in the microneedle peaks exhibited almost no fluorescence when the DNA concentration ranged from 0 to 10,000 pM (Figure 3A). By contrast, microneedles with graphene aerogels accumulated trace amounts of DNA, essentially exhibiting weak glow under a fluorescence microscope (Figure 3B). The fluorescence intensities of these microneedles were further quantified, thereby confirming significantly increased DNA adsorption by the graphene-containing microneedles (Figure S6). Notably, the amount of DNA captured by the MNAs increased with incubation time, and strong fluorescence was observed after 30 min incubation (Figure S7). Therefore, the optimal incubation time of the MNAs was 30 min in subsequent experiments. In addition, MNA was used to penetrate the agarose blocks and capture the inner fluorescent DNA (Figure S8). Strong fluorescence of the microneedle peaks was observed, thus demonstrating the desired agarose penetration and DNA capture. Additionally, laser scanning confocal microscopy (LSCM) images of the MNA further revealed that the captured fluorescent DNA was concentrated predominantly in the microneedle peaks (Figure S9).

MNA, which integrates a graphene aerogel with ideal absorption ability, a hydrogel brace with satisfactory mechanical strength, and a substrate with good hydrophobic properties, functions as a promising platform for on-tissue sampling and on-needle PCR analysis. During the entire detection process, the microneedle peaks first contacted the object to be tested and indiscriminately captured the inner DNA molecules (Figure 3C). After the MNA was removed from the tested object, PCR reaction fluids containing Scorpion probes were added, and the target DNA was amplified. By reading the fluorescence signals of the microneedle peaks, the presence of the target DNA could be detected. For a preliminary evaluation of their practical performance, MNAs were employed to identify four common lung carcinoma DNA biomarkers[40,41] in standard solutions: codon 12 mutation in KRAS exon 2 (KRAS-G12C), codon 600 mutation in BRAF exon 15 (BRAF-V600E), exon 19 deletions in EGFR (EGFR-19DEL), and exon 21 point mutation in EGFR (EGFR-L858R). The results showed that all four DNA biomarkers could be detected by the MNAs, with the microneedle peaks emitting green fluorescence (Figure 3D). Additionally, direct fluorescence quantitative PCR of the standard substance solutions was performed, which served as a reference method to verify that the detection results of the MNAs were correct (Figure S10). To further investigate the specificity and anti-interference capacity, MNAs were used to detect KRAS-G12C in a mixed solution containing other interfering genes. Evidently, the fluorescence intensity of the MNAs remained almost the same in the different groups, thus indicating the precision and specificity of this detection strategy (Figure 3E).

Remarkably, multiple PCR amplification and detection reactions could be conducted by dividing the MNA into diverse independent compartments using hydrophobic baffles. To fabricate these compartmentalized MNAs, silicone negative molds with specially designed ditches were employed, with the other procedures unchanged. Essentially, bisected and quartered MNAs were prepared as representatives, as shown in Figure S11. For bisecting the MNA, KRAS-G12C detection was performed in one compartment and exhibited green fluorescence, whereas the other was set as a blank control and exhibited no fluorescence (Figure S12). In terms of quartering MNA, the four compartments detected were KRAS-G12C, BRAF-V600E, EGFR-19DEL, and EGFR-L858R. The fluorescence intensities of the four compartments differed because the standard solutions of the four biomarkers were also different. These results indicate that these MNAs can serve as versatile DNA detection platforms.

Based on the *in vitro* detection of standard substance solutions, the ability of F-PCR-MNAs to distinguish tumors from normal tissues was tested. To acquire the desired tumor tissues, a cell line isolated from non-small cell lung cancer was transplanted into nude mice, and the developed tumor tissues were excised together with neighboring normal tissues (Figure 4A). First, whether the MNA has sufficient strength for the penetration of dense tumor tissues was corroborated by pressing the entire acquired tumor tissue (Figure S13). After removing the MNA, the traces of the microneedles remaining on the tumor tissue were photographed. Both the bright-field and fluorescence images revealed that the MNA could effectively penetrate the tumor and reach tissues as deep as 420 μm (Figure S14).

Next, another hybrid tissue containing both the tumor and normal zones was cut into 3 × 3 × 3 thin pieces. Subsequently, the MNA was pressed onto the pieces for 30 min to ensure full penetration and DNA capture, followed by EGFR-L858R detection on the F-PCR-MNA (Figures 4B–4D). The green fluorescence of the microneedle peaks in direct contact with tumor tissues demonstrated that the mutant DNA could be detected and F-PCR-MNA could be sampled in a 3D manner (Figure 4E). Specifically, the microneedle peaks penetrating normal tissues exhibited only faint fluorescence, thus indicating that F-PCR-MNA could identify small amounts of tumor tissue and differentiate between tumors and normal tissues. Moreover, the captured DNA was distributed primarily on the surface of the microneedle peaks, as shown in Figure S15. Based on these fluorescence images, the tumor sites were reconstructed both layer wise and overall (Figures 4F and 4G). The green color clearly labels the tumor zones and visually reproduces the entire tissue.

To verify the clinical value of these F-PCR-MNAs, 16 fresh patient specimens were collected from ultrasound-guided lung punctures (Figure 5A). For example, the tissue was first cut into nine small pieces and subjected to MNA for 30 min (Figure 5B). Subsequently, KRAS-G12C, BRAF-V600E, EGFR-19DEL, and EGFR-L858R detections were performed synchronously on F-PCR-MNA. The detection

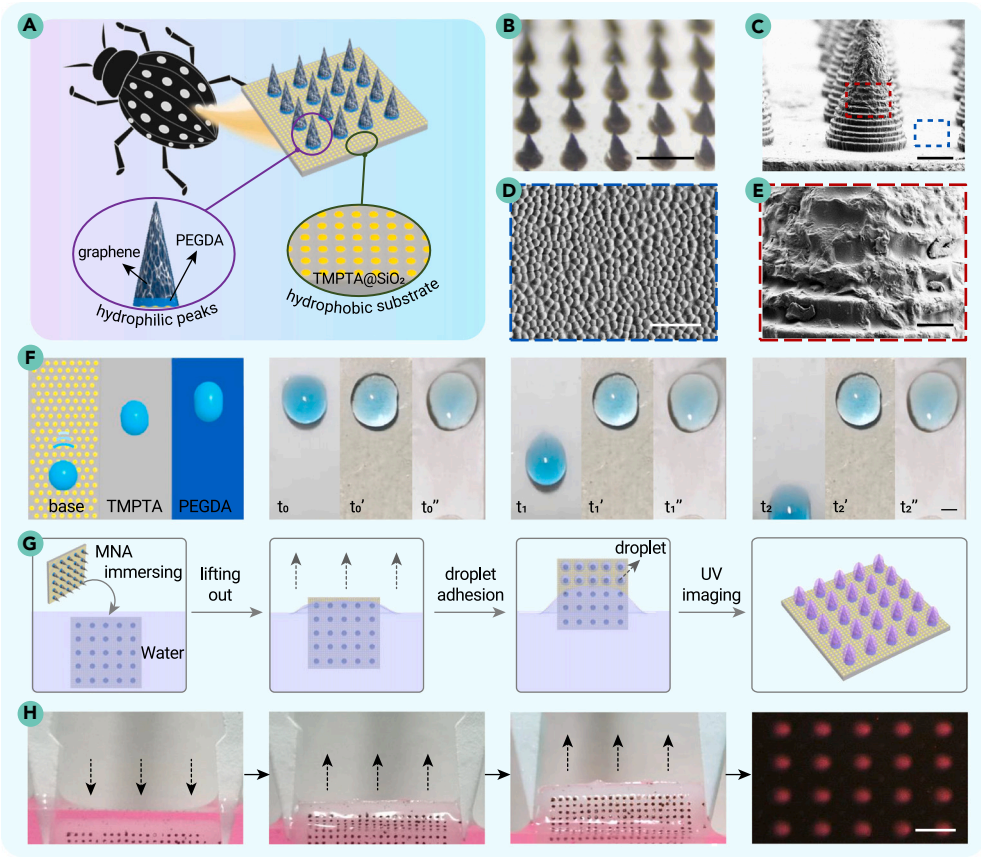

Figure 2. Characterization and properties of the MNA (A) Schematic illustrations of the composition of the MNA and its resemblance to the *Stenocara gracilipes*. (B) Optical image of the MNA. (C–E) SEM images: the MNA (C), the magnified substrate (D), and the magnified microneedle peak composed of both graphene aerogel and PEGDA hydrogel (E). (F) Schematic illustrations and time-varying images of droplets sliding down the substrate, the TMPTA plate, and the PEGDA plate. Droplets are dyed cyan and have a volume of 15 μL. $t_0 = t_0' = t_0'' = 0$ s, $t_1 = t_1' = t_1'' = 0.1$ s, $t_2 = t_2' = t_2'' = 0.15$ s. (G) Schematic illustrations of the MNA confining droplets around its microneedle peaks. (H) Optical images of the MNA being immersed in water solutions, picking up droplets, and being imaged under UV. The scale bars represent 500 μm in (B), 100 μm in (C), 2 μm in (D), 20 μm in (E), 1 mm in (F), and 400 μm in (H).

results of F-PCR-MNA are vividly reflected in the fluorescence images (Figure 5C). Compared with the lesion sites, the fluorescence of the normal sites was very weak; thus, they could be easily distinguished from each other. After sampled by MNA, the same tissues were carefully removed, immersed in paraformaldehyde overnight, dehydrated, vitrified, embedded in paraffin, sectioned, and stained with H&E. Evidently, numerous cells with enlarged, irregularly shaped, and deeply stained nuclei were spotted in the H&E staining images (Figures 5Di, 5Dii, 5Div, 5Dv, and 5Dvii–5Dix); this could preliminarily disclose the possibility of cancerization. By contrast, the detected regions in Figures 5Diii and 5Dvi were still non-cancerous. These results were consistent with the F-PCR-MNA-based detection. Notably, F-PCR-MNA-based detection was also in accordance with intraoperative fast pathology and clinical diagnosis. Intraoperative fast pathology refers to the rapid processing and regular staining of tissues during surgery, which serves as a pre-diagnosis result to guide subsequent surgery, and the clinical diagnosis is generated by doctors based on patients' imaging examination and routine pathology in the pathology department. Similar procedures were performed on another 15 lung specimens. All 16 cases, including 3 negatives and 13 positives, showed conformity between the two detection approaches, as well as intraoperative fast pathological results and clinical diagnosis (Figure 5E). These results demonstrate the reliability of these F-PCR-MNAs for practical use and indicate their potential for clinical applications.

CONCLUSION

In summary, resembling the heterogeneous back of *Stenocara gracilipes*, MNAs with anisotropic wettability were fabricated herein for 3D sampling and on-needle PCR reaction to realize efficient spatial tumor biopsy. This MNA, composed of graphene microneedle peaks, PEGDA braces, and a TMPTA@SiO_2 substrate, was manufactured by combining multiple techniques, including 3D printing, nanoparticle self-assembly, template replication, and light-induced stereolithography. With appropriate mechanical strength, the hydrogel brace facilitated tumor tissue penetration and stereoscopic sampling. Meanwhile, the graphene aerogel enabled the MNA to rapidly collect and capture DNA biomarkers, whereas the hydrophobic substrate contributed to the replacement of reaction fluids, independence of detection, and a decrease in background fluorescence. By integrating these attributes, the F-PCR-MNAs were able to detect four typical lung cancer DNA biomarkers from standard substance solutions in a specific, precise, intuitive, and flexible manner. In addition, animal experiments demonstrated that F-PCR-MNAs can detect hidden tumors from a large piece of tissue. The accurate tumor diagnosis of several patient-derived samples via F-PCR-MNAs further indicates the practical value and clinical prospects of this spatial tumor biopsy strategy.

Compared with traditional histopathology staining methods (Figure S16), the presented F-PCR-MNA-based diagnosis has several advantages as listed in Table S1. Essentially, this technique collects biomarkers directly from the tissue in a 3D omnidirectional manner; furthermore, it reports detection results visually, precisely, and efficiently. Thus, tedious slicing processes (such as tissue fixation, washing, embedding, and slicing via microtome) and slice-by-slice microscopic examination can be omitted. In addition, given that the operations rely primarily on a PCR amplifier and a fluorescent reading device, they are relatively simple for non-specialists. Additionally, the F-PCR-MNA platform is functional and suitable for tumor heterogeneity, with the potential to locate tumor sites and identify gene mutations. In terms of economic cost, the cost of MNA fabrication is low, and the cost of the entire platform is very close to that of traditional PCR tests.

However, because cfDNA from tumor cells is distributed throughout the surrounding tissues, the first-generation F-PCR-MNAs presented in this proof-of-concept work are still unable to realize the accurate localization of tumor cells or 3D reconstruction analysis of the suspicious tissue. To achieve this goal, MNAs may have to be scaled down to the nanometer scale to capture DNA markers directly inside cells. In addition to these improvements, the F-PCR-MNAs can be integrated with sampling equipment such as puncture needles, biopsy forceps, and endoscopes to avoid the procedures of tissue storage and transport, thus saving considerable time and manpower. Additionally, future work will be conducted to allow graphene to occupy more space in the microneedle peaks to guarantee sufficient biomarker capture throughout these peaks. For this purpose, a higher-concentration graphene-dispersed solution can be used to fabricate graphene aerogels with increased volume and content. Another way to increase the graphene distribution is to use porous hydrogels containing high graphene concentrations, which can be fabricated by adding pore-forming agents or directional freezing as the peak material. With these benefits and advancements, this F-PCR-MNA-based strategy is expected to be applied for clinical diagnosis of various cancers and to promote the development of super-fast tumor detection technologies.

MATERIALS AND METHODS

Fluorosilane modification on silica nanoparticles

In brief, 10 g SiO_2 nanoparticles were dissolved in 100 mL ethanol via ultrasonic dispersion, and 1 mL 1H,1H,2H,2H-perfluorodecyltriethoxysilane (PFDTES) was added. The mixed solution was vigorously stirred for 4 h. To obtain the TMPTA@SiO_2 solution, the mixture was

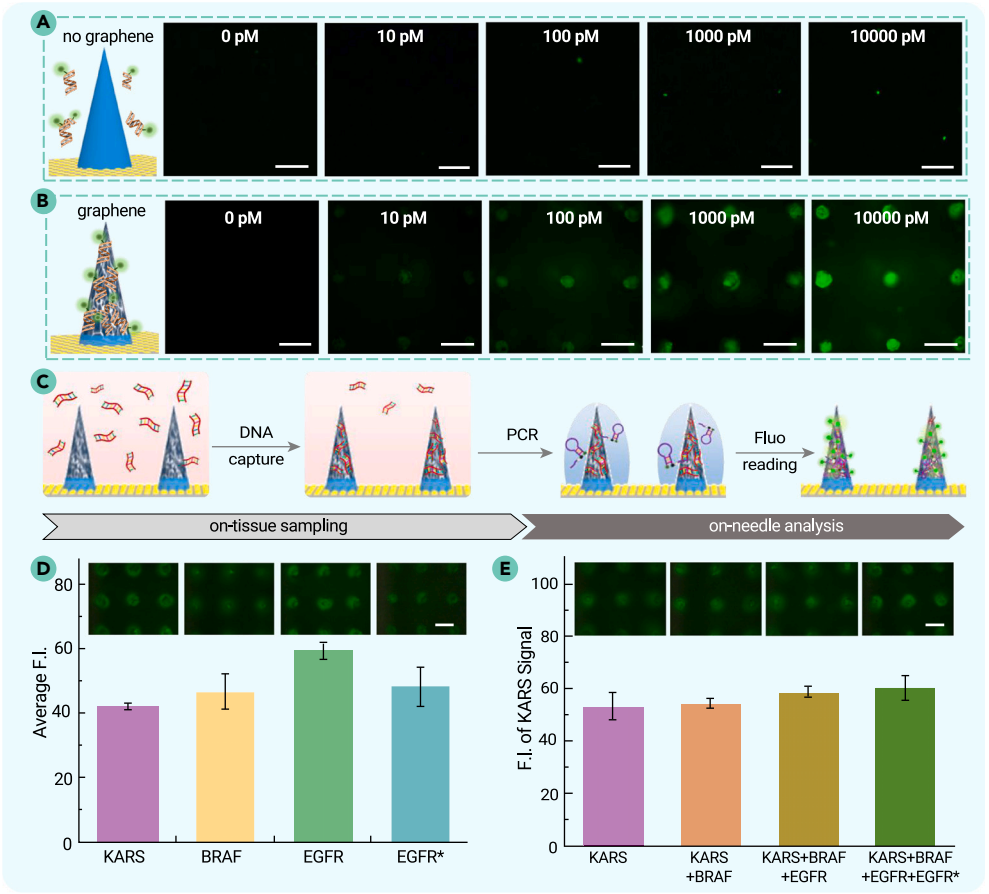

Figure 3. DNA capture and detection abilities of MNAs (A and B) Abilities of microneedle peaks without graphene aerogel (A) and with graphene aerogel (B) to enrich fluorescence-labeled DNA. The DNA concentrations vary from 0 to 10,000 pM. (C) Schematic illustrations of F-PCR-MNA-based detection of lung carcinoma DNA biomarkers in standard substance solutions. Fluo., fluorescence. (D) Fluorescence images and corresponding fluorescence intensities of microneedle peaks after detecting KARS (KRAS-G12C), BRAF (BRAF-V600E), EGFR (EGFR-19DEL), and EGFR* (EGFR-L858R). F.I., fluorescence intensity. n = 4. (E) Fluorescence images and corresponding fluorescence intensities of microneedle peaks after detecting KARS in mixed solutions with interfering DNA. n = 4. Student's t test was performed by comparing the KARS group with other groups. NS, not significant. All scale bars represent 200 μm.

blended with TMPTA pre-polymer at a certain ratio by vortex oscillation. After evaporating the ethanol in an oven (at 75°C overnight), the TMPTA@SiO_2 solution was prepared.

Fabrication of F-PCR-MNA

A 49 × 49 microneedle template array was generated using a 3D printer (Markforged). The microneedle height, microneedle basal diameter, intermicroneedle distances, substrate sizes, and material compositions were 500 μm, 250 μm, 400 μm, 20 × 20 × 1.8 mm^3, and nylon plastic, respectively. Subsequently, polydimethylsiloxane (PDMS) with 10% (v/v) curing agents was poured on the microneedle template, and the template was cured at 60°C overnight. Thus, the silicone negative mold with a complementary shape was constructed. Next, 20 mg/mL graphene dispersed solution was filled in the cavities of the negative mold via vacuum treatment for 10 min three times. After removing the extra dispersed solution, the solutions remaining in the cavities were reacted with 10% (w/v) $CaCl_2$ for 30 min. Subsequently, they were held at −80°C overnight and freeze dried in a lyophilizer (Biocool). A 50% (v/v) PEGDA solution mixed with 1% (v/v) 2-hydroxy-2-methylpropiophenone (HMPP) was added to the graphene aerogels and vacuum treated. The redundant PEGDA solution was discarded, and the residual solution was solidified via ultraviolet (UV) irradiation (365 nm) for 30 s. Subsequently, the TMPTA pre-polymer containing 1% (v/v) HMPP and 10% (w/v) fluorosilane-modified silica nanoparticles was then added, connected to PEGDA, and polymerized under UV light (365 nm) for 3 min. The MNA was fabricated by peeling off the negative silicone mold.

Compression tests

To conduct the compression tests, graphene aerogels were made into cylindrical blocks with a bottom diameter of 5 mm and a height of 2.5 mm using the same methods as the $CaCl_2$ treatment and freeze drying. Half of the blocks were fused with PEGDA hydrogels by submerging them in a PEGDA solution (50%, v/v) overnight, removing them, and solidifying them under UV light (365 nm, 30 s). An electronic material testing system (INSTRON) was employed to record real-time forces. The pressure was measured according to the user's manual, and the moving speed was set to 1 mm/min.

Wettability tests

Three types of polymer plates were used for wettability tests: PEGDA, TMPTA, and TMPTA plates containing 10% (w/v) fluorosilane-modified silica nanoparticles. Contact angles were measured using a contact angle meter (Hitachi, CA-A) with 2 μL dH_2O droplets at room temperature. The sliding experiments were performed by dripping cyan-dyed dH_2O droplets with a volume of 15 μL on the plates with a slope of approximately 45°. Real-time photographs were recorded using a camera (Huawei P30pro).

Droplet picking up tests

To observe the behavior of each microneedle peak more carefully, 20 × 20 MNAs with large intermicroneedle distances were used. The MNA was vertically immersed in a red fluorescent water solution for 5 s before it was slowly removed. After the extra solution flowed away, a top-view fluorescence image of the microneedle peaks surrounded by droplets was captured under UV irradiation (365 nm) using a charge-coupled device (CCD) camera (Oplenic) connected to a stereomicroscope (Jiangnan).

Capture of fluorescence-labeled DNA

Fluorescence-labeled DNA solutions at concentrations of 0, 10, 100, 1,000, and 10,000 pM were prepared for later use. To determine the optimal incubation time, the MNA was immersed in 1,000 pM DNA solutions at 37°C for 5, 10, 15, 20, 30, and 40 min. To compare the DNA absorption effects, MNAs and microneedles without graphene aerogels were immersed in the above DNA solutions at 37°C for 30 min. After incubation, the remaining DNA was removed by adsorbing it onto the paper. Fluorescent images were obtained using an inverted fluorescence microscope (Leica DMi8).

Detection of DNA biomarkers in standard substance solutions

Four standard substances were used in the experiments: KRAS-G12C, BRAF-V600E, EGFR-19DEL, and EGFR-L858R; these standards were diluted 1,000 times with dH_2O beforehand. MNAs were incubated with the standard substance solutions at 37°C for 30 min. Subsequently, they were removed, and the excess solution was removed using an absorbing paper. After being dipped in the PCR fluids, the MNAs were placed upside down in a glass dish, and paraffin oil was added for sealing. The entire system was placed in a PCR amplifier whose customized heating platform had a specific concave shape to hold the glass dish (Life Technologies, 2720 Thermal Cycler). The amounts of different reaction liquids and settings of the PCR program were determined according to the manufacturer's instructions. Finally, the reaction fluids were removed, and fluorescence images of the MNAs were examined using an inverted fluorescence microscope (Leica, DMi8). Diluted standard substances were detected using fluorescent quantitative PCR as reference.

Fabrication of compartmentalized F-PCR-MNAs

The fabrication procedure for the compartmentalized MNAs was similar to that described above. By contrast, negative silicone molds with specially designed ditches, which were fabricated by carving the original negative molds, were employed. For bisecting the MNAs, the ditch was on the centerline, whereas for quartering the MNAs, the ditches were on the diagonals. Other surgical procedures were unaltered.

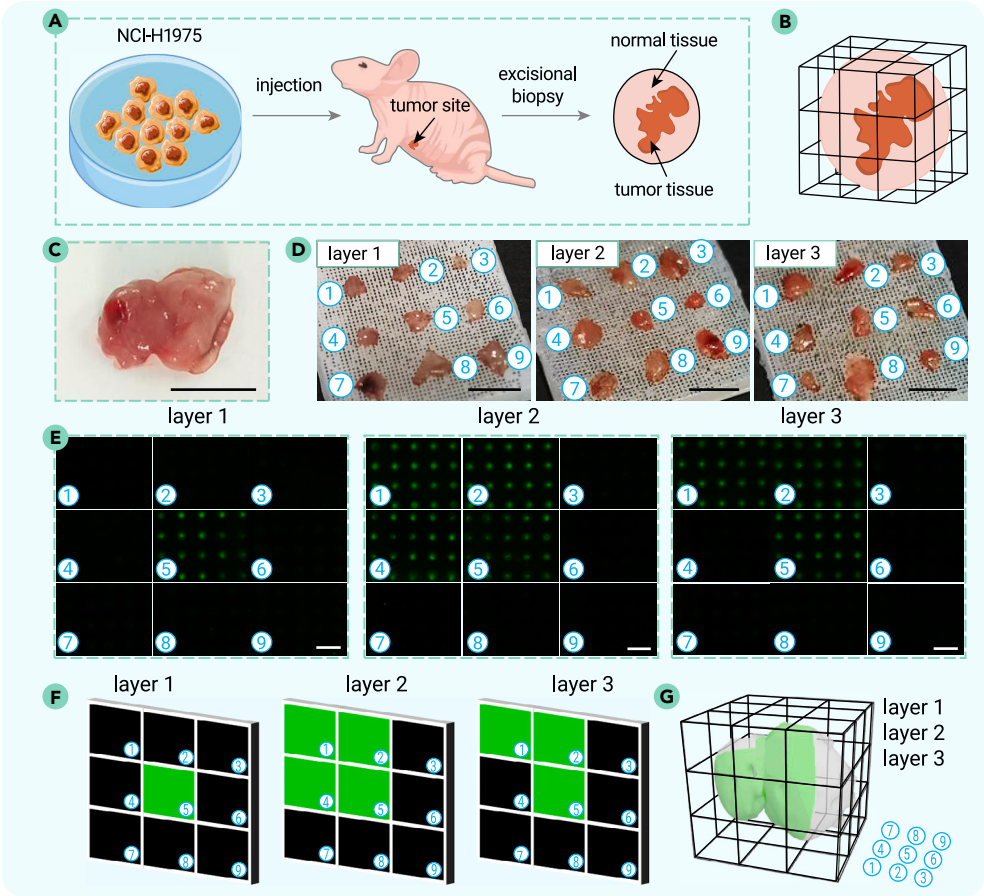

Figure 4. ***In vivo*** **detection of mouse tissue samples**
(A) Schematic illustrations of the acquisition of mouse tumor tissues. (B) Schematic illustration of tissue segmentation. (C) Optical image of the tumor tissue enclosed by normal tissue. (D) Optical images of the MNAs bearing mouse tumor tissues and normal tissues. The hybrid tissue is cut into 3 × 3 × 3 pieces, with the tumor tissues labeled as no. 5 of layer 1, nos. 1, 2, 4, and 5 of layer 2, and nos. 1, 2, and 5 of layer 3. (E) Corresponding fluorescence images of the microneedle peaks to show the results. (F) 3D reconstruction of each layer (tumor sites: green; normal sites: black). (G) 3D reconstruction of the entire tissue (tumor sites: green; normal sites: gray). The scale bars represent 0.5 cm in (C) and (D) and 500 μm in (E).

Penetration tests

Before the penetration tests, 5% agarose blocks of 1 × 1 × 0.5 cm^3 were immersed in 1,000 pM fluorescence-labeled DNA solution overnight, and tumor tissues were excised from mice 10 days after model establishment. MNAs were pressed on the agarose blocks and tumor tissues via a microneedle injector (EFL, Suzhou, China), respectively, and then placed at 37°C for 30 min. Bright-field images were captured using a camera phone (Huawei P30pro). Fluorescence images of the MNAs after capturing the DNA in the agarose blocks were recorded using an inverted fluorescence microscope (Leica DMi8). LSCM images were obtained using a laser scanning confocal microscope (Olympus FV3000).

Detection of tumor tissues from nude mouse models

Tumor tissues that grew for 3 days in mice were excised together with neighboring normal tissues for detection (tumor size, <0.15 cm^3). The samples were cut into small pieces (<0.01 cm^3), pressed by MNAs via the microneedle injector (approximately 8 N), and incubated in a moist environment at 37°C for 30 min immediately after their acquisition. The kits for EGFR-L858R detection were used, and the MNAs were subjected to the same detection process as previously described. Fluorescence and LSCM images were obtained using an inverted fluorescence microscope (Leica, DMi8) and a laser scanning confocal microscope (Olympus, FV3000), respectively. 3D reconstruction was performed using a scanner and the 3D MAX 2021 software. Specifically, a scanner was used to capture the front, back, left, right, top, and bottom images of the tissue. Based on these images, an outline of the tissue was drawn.

Detection of clinical specimens

Sixteen patient-derived specimens were acquired via ultrasound-guided lung puncture at the Drum Tower Hospital, with informed consent from the patient. Most parts of the specimen were used for clinical diagnosis, and a small segment was used for microneedle detection. Detection was performed within 12 h of retrieval. The tissue segments (<0.05 cm^3) were further cut into small pieces (<0.006 cm^3), pressed by MNAs via the microneedle injector (approximately 8 N), and then incubated in a moist environment at 37°C for

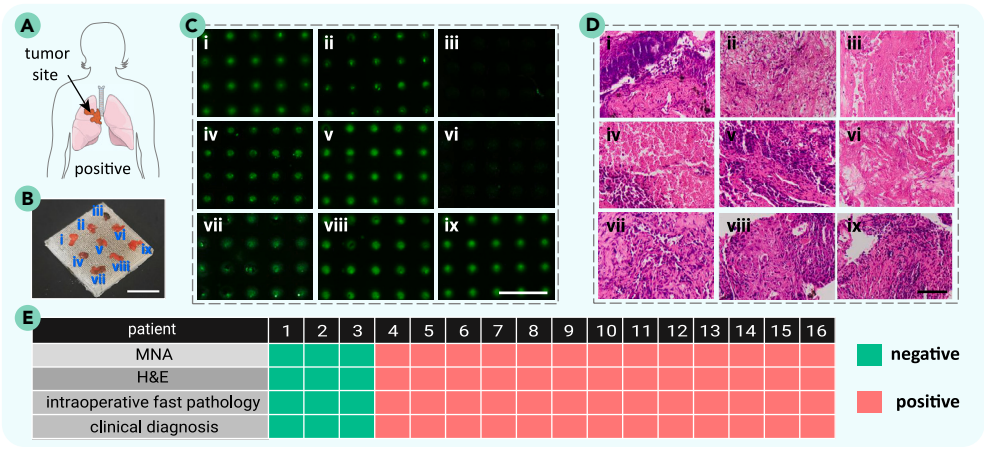

Figure 5. ***In vivo*** **detection of clinical patient specimens**
(A) Schematic illustration of the source of patient specimens. (B) Optical image of the MNA bearing the sliced tissues from one patient specimen (i–ix). (C) Corresponding fluorescence images of the microneedle peaks to show the results. (D) Corresponding H&E staining images of the sliced tissues after they are removed from the MNA. (E) Colored table showing the conformity of F-PCR-MNA-based detection, H&E staining, intraoperative fast pathology, and clinical diagnosis of 16 patient specimens. The scale bars represent 1 cm in (B), 800 μm in (C), and 50 μm in (D).

30 min. KRAS-G12C, BRAF-V600E, EGFR-19DEL, and EGFR-L858R were detected as previously described. Fluorescent images were obtained using an inverted fluorescence microscope (Leica DMi8). In addition, immediately after their careful removal from the MNAs, the tissue segments were immersed in paraformaldehyde overnight, dehydrated by graded ethanol, vitrified by dimethylbenzene, embedded in paraffin, and cut into 5 μm slices for H&E staining.

REFERENCES

1. Wu, L., Ishigaki, Y., Hu, Y., et al. (2020). H_2S-activatable near-infrared afterglow luminescent probes for sensitive molecular imaging in vivo. Nat. Commun. ***11***, 446.
2. Chen, J., Jiang, Z., Zhang, Y.S., et al. (2021). Smart transformable nanoparticles for enhanced tumor theranostics. Appl. Phys. Rev. ***8***, 041321.
3. Liu, Y., Wang, J., Xiong, Q., et al. (2021). Nano-bio interactions in cancer: from therapeutics delivery to early detection. Acc. Chem. Res. ***54***, 291–301.
4. Wu, D., Chi, J., Zhang, M., et al. (2022). Water-dispersing perovskite probes for the rapid imaging of glioma cells. Adv. Opt. Mater. ***10***, 2101835.
5. Zhang, Y., Tu, J., Wang, D., et al. (2018). Programmable and multifunctional DNA-based materials for biomedical applications. Adv. Mater. ***30***, 1703658.
6. Crosby, D., Bhatia, S., Brindle, K.M., et al. (2022). Early detection of cancer. Science ***375***, eaay9040.
7. Zhao, M., Mi, D., Ferdows, B.E., et al. (2022). State-of-the-art nanotechnologies for the detection, recovery, analysis and elimination of liquid biopsy components in cancer. Nano Today ***42***, 101361.
8. Kim, E.S., Velcheti, V., Mekhail, T., et al. (2022). Blood-based tumor mutational burden as a biomarker for atezolizumab in non-small cell lung cancer: the phase 2 B-F1RST trial. Nat. Med. ***28***, 939–945.
9. Ji, X., Ge, L., Liu, C., et al. (2021). Capturing functional two-dimensional nanosheets from sandwich-structure vermiculite for cancer theranostics. Nat. Commun. ***12***, 1124.
10. Haddad, T.S., Friedl, P., Farahani, N., et al. (2021). Tutorial: Methods for three-dimensional visualization of archival tissue material. Nat. Protoc. ***16***, 4945–4962.
11. He, J., Chen, C., Chen, L., et al. (2022). Honeycomb-like hydrogel microspheres for 3D bulk construction of tumor models. Research ***2022***, 9809763.
12. Zhao, T., Chiang, Z.D., Morriss, J.W., et al. (2022). Spatial genomics enables multi-modal study of clonal heterogeneity in tissues. Nature ***601***, 85–91.
13. Patel, K.B., Liang, W., Casper, M.J., et al. (2022). High-speed light-sheet microscopy for the in-situ acquisition of volumetric histological images of living tissue. Nat. Biomed. Eng. ***6***, 569–583.
14. Balaur, E., O' Toole, S., Spurling, A.J., et al. (2021). Colorimetric histology using plasmonically active microscope slides. Nature ***598***, 65–71.
15. Zhang, D., Deng, Y., Kukanja, P., et al. (2023). Spatial epigenome–transcriptome co-profiling of mammalian tissues. Nature ***616***, 113–122.
16. Wirth, J., Huber, N., Yin, K., et al. (2023). Spatial transcriptomics using multiplexed deterministic barcoding in tissue. Nat. Commun. ***14***, 1523.
17. Jamaledin, R., Yiu, C.K.Y., Zare, E.N., et al. (2020). Advances in antimicrobial microneedle patches for combating infections. Adv. Mater. ***32***, 2002129.
18. Zhang, X., Chen, G., Bian, F., et al. (2019). Encoded microneedle arrays for detection of skin interstitial fluid biomarkers. Adv. Mater. ***31***, 1902825.
19. Yang, J., Zhang, H., Hu, T., et al. (2021). Recent advances of microneedles used towards stimuli-responsive drug delivery, disease theranostics, and bioinspired applications. Chem. Eng. J. ***426***, 130561.
20. Wang, Z., Luan, J., Seth, A., et al. (2021). Microneedle patch for the ultrasensitive quantification of protein biomarkers in interstitial fluid. Nat. Biomed. Eng. ***5***, 64–76.
21. Yi, K., Wang, Y., Shi, K., et al. (2021). Aptamer-decorated porous microneedles arrays for extraction and detection of skin interstitial fluid biomarkers. Biosens. Bioelectron. ***190***, 113404.
22. Keyvani, F., Zheng, H., Kaysir, M.R., et al. (2023). A hydrogel microneedle assay combined with nucleic acid probes for on-site detection of small molecules and proteins. Angew. Chem. Int. Ed. ***62***, e202301624.
23. Tehrani, F., Teymourian, H., Wuerstle, B., et al. (2022). An integrated wearable microneedle array for the continuous monitoring of multiple biomarkers in interstitial fluid. Nat. Biomed. Eng. ***6***, 1214–1224.
24. Paul, R., Ostermann, E., Chen, Y., et al. (2021). Integrated microneedle-smartphone nucleic acid amplification platform for in-field diagnosis of plant diseases. Biosens. Bioelectron. ***187***, 113312.
25. Chen, L., Ding, J., Yuan, H., et al. (2022). Deep-dLAMP: Deep learning-enabled polydisperse emulsion-based digital loop-mediated isothermal amplification. Adv. Sci. ***9***, 2105450.
26. Sun, C., Liu, L., Pérez, L., et al. (2022). Droplet-microfluidics-assisted sequencing of HIV proviruses and their integration sites in cells from people on antiretroviral therapy. Nat. Biomed. Eng. ***6***, 1004–1012.
27. Al Sulaiman, D., Juthani, N., and Doyle, P.S. (2022). Quantitative and multiplex detection of extracellular vesicle-derived microRNA via rolling circle amplification within encoded hydrogel microparticles. Adv. Healthc. Mater. ***11***, 2102332.
28. Song, P., Wu, L.R., Yan, Y.H., et al. (2022). Limitations and opportunities of technologies for the analysis of cell-free DNA in cancer diagnostics. Nat. Biomed. Eng. ***6***, 232–245.
29. Wang, Z., and Cui, W. (2020). CRISPR-Cas system for biomedical diagnostic platforms. View ***1***, 20200008.
30. Wei, Q., Arami, H., Santos, H.A., et al. (2021). Intraoperative assessment and photothermal ablation of the tumor margins using gold nanoparticles. Adv. Sci. ***8***, 2002788.
31. Herberts, C., Annala, M., Sipola, J., et al. (2022). Deep whole-genome ctDNA chronology of treatment-resistant prostate cancer. Nature ***608***, 199–208.
32. Zhang, X., Sun, L., Wang, Y., et al. (2019). Multibioinspired slippery surfaces with wettable bump arrays for droplets pumping. P. Natl. Acad. Sci. USA ***116***, 20863–20868.
33. Zhang, H., Zhao, G., Wu, S., et al. (2021). Solar anti-icing surface with enhanced condensate self-removing at extreme environmental conditions. P. Natl. Acad. Sci. USA ***118***, e2100978118.
34. Li, H., Li, A., Zhao, Z., et al. (2021). Precise droplet manipulation based on surface heterogeneity. Acc. Mater. Res. ***2***, 230–241.
35. Bian, F., Sun, L., Cai, L., et al. (2020). Bioinspired MXene-integrated colloidal crystal arrays for multichannel bioinformation coding. P. Natl. Acad. Sci. USA ***117***, 22736–22742.
36. Pang, K., Song, X., Xu, Z., et al. (2020). Hydroplastic foaming of graphene aerogels and artificially intelligent tactile sensors. Sci. Adv. ***6***, eabd4045.
37. Wang, B., Zhang, S., Meng, J., et al. (2021). Evaporation-Induced rGO coatings for highly sensitive and non-invasive diagnosis of prostate cancer in the PSA gray zone. Adv. Mater. ***33***, 2103999.
38. Wu, S., Liang, Z., Li, Y., et al. (2022). Transparent, photothermal, and icephobic surfaces via layer-by-layer assembly. Adv. Sci. ***9***, 2105986.
39. Liu, F., Yang, Y., Wan, X., et al. (2022). Space-confinment-enhanced fluorescence detection of DNA on hydrogel particles array. ACS Nano ***16***, 6266–6273.
40. Chaudhuri, A.A., Chabon, J.J., Lovejoy, A.F., et al. (2017). Early detection of molecular residual disease in localized lung cancer by circulating. Cancer Discov. ***7***, 1394–1403.
41. Mathios, D., Johansen, J.S., Cristiano, S., et al. (2021). Detection and characterization of lung cancer using cell-free DNA fragmentomes. Nat. Commun. ***12***, 5060.

ACKNOWLEDGMENTS

This work was supported by the National Key Research and Development Program of China (2020YFA0908200); the National Natural Science Foundation of China (T2225003 and 52073060); the Clinical Trials from Nanjing Drum Tower Hospital (2022-LCYJ-ZD-01); the Nanjing Medical Science and Technique Development Foundation (ZKX21019); the Guangdong Basic and Applied Basic Research Foundation (2021B1515120054); and the Shenzhen Fundamental Research Program (JCYJ20190813152616459 and JCYJ20210324133214038).

AUTHOR CONTRIBUTIONS

Y.Z. devised the idea and revised the introduction part. X.Z. designed the architecture, conducted the experiments, and wrote the manuscript. G.C. analyzed the data and revised the manuscript. Y.W. helped with data analysis, participated in scientific discussion, and checked the grammar.

DECLARATION OF INTERESTS

The authors declare no competing interests.

SUPPLEMENTAL INFORMATION

It can be found online at https://doi.org/10.1016/j.xinn.2023.100538.

LEAD CONTACT WEBSITE

www.zhaoyuanjin.com.